

# Numerical study of the coupling between the instantaneous blade loading/power of an axial wind turbine and upstream turbulence at high Reynolds numbers

Mohammad H. B. Ahmadi<sup>a,\*</sup>, Zhiyin Yang<sup>a</sup>

<sup>a</sup>*School of Mechanical Engineering and the Built Environment, University of Derby, Derby DE22 3AW, UK*

---

## Abstract

Little is known about how the range of scales in the approaching turbulent flow can interact dynamically with wind turbines and influence its ability to produce power. Here, a numerical study of a horizontal-axis wind turbine at different Reynolds numbers (corresponding to different tip speed ratios) has been conducted to investigate the instantaneous turbine response to upstream turbulence. A computational approach, combining large eddy simulation with actuator line modelling, is adopted. Comparison between Power Spectral Density (PSD) of the turbine thrust/power and PSD of the velocity at the rotor plane and one rotor diameter upstream of it confirms that there is a coupling between the instantaneous turbine thrust/power and the upstream turbulence (1 D upstream of the turbine) for frequencies below a critical frequency. Furthermore, it has been shown for the first time, that PSD of the turbine thrust/power and the velocity PSD at the rotor plane are very similar, indicating that the instantaneous turbine thrust/power and the velocity at the rotor plane are coupled for all frequencies. This means that the PSD of velocity at the rotor plane or shortly behind it can provide interesting information for the instantaneous turbine loads that are very important for the turbine operational life.

*Keywords:*

Wind turbine, LES, ALM, Frequency analysis, Power, Blade loads

---

## 1. Introduction

Wind energy is currently the fastest-growing energy source in the world. However, before large scale wind farms can utilize the wind's energy potential, there are still many scientific and technical challenges to be addressed, especially that our current understanding of the effects of unsteady approaching flow on turbine performance and power is poor, and there are no robust numerical tools for accurate prediction of unsteady blade loading which strongly affect the turbine operational life. Unsteady loading on blades, and hence on the turbine, is due to the rotation of the blades through an unsteady incoming flow and in proximity to a fixed support structure. The upstream turbulence also leads to strong temporal variations of the power output of individual wind turbines and of the entire farm [1]. The influence of these factors on wind turbine design has received attention through experimental studies such as the European Union project "Model Experiments in Controlled Conditions" (MEXICO) [2, 3, 4], model-based optimization approaches [5] and computational analysis using Large Eddy Simulation (LES) approach [6, 7, 8] which is particularly suited to complex unsteady flows and plays an important role in providing useful data besides wind tunnel and field experimental data [9]. Such studies has led to the development of useful engineering tools for predicting unsteady loads and component load spectra [10, 11] that are required for fatigue design.

Another key question is that how the range of scales in the approaching turbulent flow can interact dynamically with the device and influence its ability to produce power. This question, which is obviously of critical significance for determining the performance of a real-life wind turbine, is still not well understood although a few studies focused on maximizing power and reducing the effect of wind on wind turbine loadings have been carried out [12, 13]. Similarly, little is known about how the dynamics of large-scale coherent motions affect the rate of wake recovery of axial-flow wind turbines.

A good understanding of the above points is particularly relevant to wind farms since in turbine arrays, the flow approaching downstream turbines will be determined by the far wake of upstream turbines which are characterised by a velocity deficit, increased turbulence intensities and a vast range of turbulence/motion scales. It has been shown that complex interactions between downstream turbines affect the total-power variations of the wind farm in the intermediate to low frequency range [14]. This can significantly influence turbine farm operation with decreased power output and increased fatigue loading of devices [15]. Observations by Neustadter [16] and Barthelmie *et al.* [17] suggest that wake related losses can reduce a wind farm's average power output by 10%. It has been shown that the wind farm power output is strongly sensitive to small variations of the wind direction and it should be taken into account for the optimal control and grid integration of wind farms [18]. Numerical studies by Porté-Agel *et al.* [19], and the observations of Hansen *et al.* [20] indicate that power losses can reach over 40% for a particular single wind direction.

---

\*Corresponding author: Mohammad H. B. Ahmadi

Email addresses: m.ahmadi@derby.ac.uk (Mohammad H. B. Ahmadi), z.yang@derby.ac.uk (Zhiyin Yang)

Increased fluctuations in power output and turbine loads can be significant in some conditions, which has also been observed in measured data [17]. Experimental studies have shown that load spectra are correlated to spectral density of the upstream flow velocity below a critical frequency close to the turbine rotational frequency but become uncorrelated at higher frequencies above that [21, 22, 23, 24]. To the authors' best knowledge, there is no other published numerical work investigating this frequency dependency and published experimental works studying this dependency only cover low to moderate turbine diameter-based Reynolds number flows ( $Re_T \leq 9.75 \times 10^5$ ).

Obtaining important parameters of wind turbines in complex flows, such as power production, turbine fatigue life and peak velocities, is complicated and requires the use of complex experimental methods or very sophisticated computational fluid dynamics (CFD) tools. Among CFD tools LES is the most feasible one at the moment for predicting unsteady turbulent flows accurately [25, 26, 27], and actuator methods have been demonstrated to be able to model time-dependent loading on turbine rotors [28, 29]. Since the combination of LES and Actuator Line Modelling (ALM) has been successful in modelling turbine wakes [30, 31], the hybrid LES/ALM approach has been employed in the present study. The CFD approach used in this study has already been validated by the authors in simulating horizontal axis tidal stream turbines [32, 33].

This study aims to advance our current understanding of the instantaneous turbine response to turbulence in the incoming flow at different Tip Speed Ratios (TSR) particularly at high Reynolds numbers ( $3.15 \times 10^6 \leq Re_T \leq 7.45 \times 10^6$ ) for an axial-flow wind turbine. The paper is structured as follows: the numerical approach used in the present study and computational details are presented in Section 2. Section 3 shows the predicted mean results and comparison against experimental data, and further analysis of instantaneous flow fields. Concluding remarks are presented in Section 4.

## 2. Numerical methodology

### 2.1. Large eddy simulation

In LES large scale turbulent motions, called large eddies, are captured directly and the effects of small scale motions are modelled using a sub-grid-scale (SGS) model. The three-dimensional (3D) instantaneous governing equations for large scale motions are obtained by applying a low-pass spatial filter to the 3D instantaneous conservation equations (Navier-Stokes) derived from the fundamental conservation laws for mass, momentum and energy. The LES governing equations are fairly standard and will be briefly described here.

The filtered equations expressing conservation of mass and momentum for incompressible flow can be written in conservative form as:

$$\begin{aligned} \frac{\partial \bar{u}_i}{\partial x_i} &= 0 \\ \frac{\partial \bar{u}_i}{\partial t} + \frac{\partial (\bar{u}_i \bar{u}_j)}{\partial x_j} &= -\frac{1}{\rho} \frac{\partial \bar{p}}{\partial x_i} + \nu \frac{\partial^2 \bar{u}_i}{\partial x_j^2} + \frac{\partial \tau_{ij}}{\partial x_j} + f_{i,\epsilon} \end{aligned} \quad (1)$$

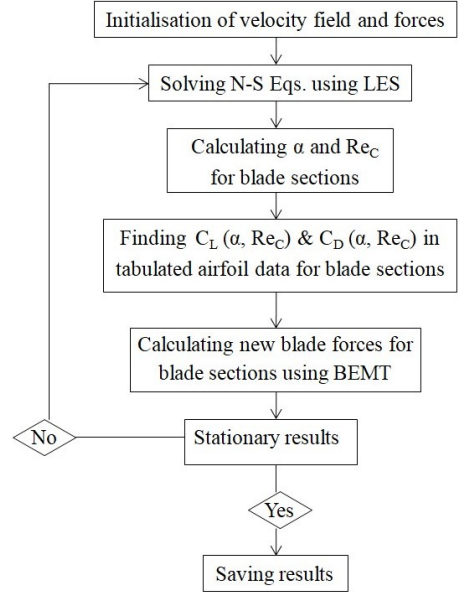


Figure 1: The hybrid LES/ALM methodology.

where the bar denotes filtering and  $f_{i,\epsilon}$  is the body force calculated from the ALM technique described briefly below in Section. 2.2. The sub-grid scale turbulent stresses are modelled with an SGS eddy viscosity as:

$$\tau_{ij} = -\nu_t \left( \frac{\partial \bar{u}_i}{\partial x_j} + \frac{\partial \bar{u}_j}{\partial x_i} \right) + \frac{2}{3} k \delta_{ij} \quad (2)$$

where  $\nu_t$  and  $k$  denote the eddy viscosity and SGS kinetic energy respectively and in this study are determined using the one-equation eddy viscosity model in which an extra equation for the SGS kinetic energy [34] is solved. The filtered governing equations are solved using the CFD code library OpenFOAM [35].

### 2.2. Actuator line modelling

In the present study, the geometry of the turbine blades is not directly resolved but modelled using the ALM method originally developed by Sørensen & Shen [36]. In the ALM technique, turbine blades are represented by rotating actuator lines and body forces equal and opposite to the lift and drag forces experienced by the turbine blades are distributed along those rotating actuator lines. The LES governing equations are solved initially at each time step to obtain the flow field. With the availability of the flow field and the blade geometry, the loads on each blade section can be calculated using a blade element approach combined with tabulated 2D aerofoil data, i.e.,  $C_L$  and  $C_D$  as functions of chord-based Reynolds number ( $Re_C$ ) and angle of attack ( $\alpha$ ). A correction factor introduced by Shen *et al.* [37] is applied on the computed 2D forces to take 3D rotational effects into account. The corrected body forces are then projected smoothly along the rotating actuator lines and neighbouring mesh points using a Gaussian function to avoid singular behaviour and numerical instability. In the present study, the Gaussian cut-off parameter is constant and has a value

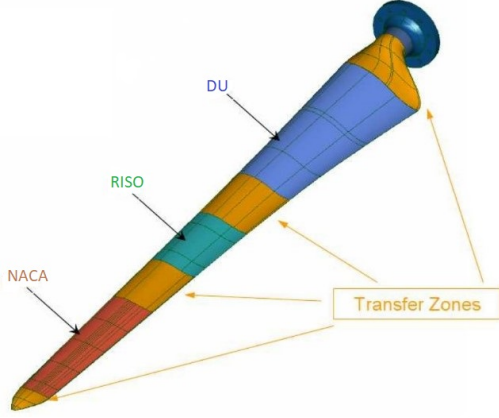


Figure 2: The blade geometry [39].

between 2 and 3 cell sizes [30]. Figure 1 presents a flowchart summarising the hybrid LES/ALM methodology. Details of the ALM technique used in the present study can be found in Ref. [32, 33].

### 2.3. Computational domain

The computations of a horizontal axis small scale wind turbine comprising of three blades with a 4.5 m diameter have been carried out using the hybrid LES/ALM approach. The geometry and flow conditions in the present study are based on the experimental set up of the European Union project 'MEXICO', Mexnext (Phase 1) [38, 2]. In the MEXICO turbine, each blade is composed of a cylinder, the inner 4.4 % of the span; a DU91-W2-250 airfoil, from 11.8 % to 40 % span; a RISOE-A1-21 airfoil, from 50 % to 62 % span and a NACA 64-418 airfoil, from 72 % to 100 % span, with three transitional zones between the airfoils. The geometric properties of the blades are summarised in Table 1 [39]. Figure 2 shows geometry of the blade used in the experiments. Since the 2D characteristic data of the Risø airfoil are very different from those of the other two airfoils and as a consequence, the measured 2D airfoil data do not correspond to the actual characteristics of the rotor, in the middle of the blade, the airfoil data modified and recommended by Shen *et al.* [37] is employed here.

Regarding the turbine geometry, in this study, the blades are not resolved and using the ALM technique, each blade is represented by a rotating actuator line in which each point on the line represents a section of the blade at the corresponding radius. The tower is ignored and nacelle is replaced by a cylinder with the same length and diameter;  $L_C = 3.95$  m and  $D_C = 0.54$  m. The simulations have been performed for three flow conditions at zero yaw angles with details listed in Table 2 where  $\Omega$  denotes the angular velocity with clockwise direction when looking downwind,  $Re$  presents the turbine diameter-based Reynolds number and  $\theta_p$  is the pitch angle.

The computational domain of  $14D \times 10D \times 10D$  is used in the present study, where  $D$  is the rotor diameter. A Cartesian structured mesh of  $5.25 \times 10^6$  grid points with a resolution nearly  $D/60$  in the turbine plane is used for the simulations. Figure 3 shows a perspective view of the computational

Table 1: Geometric properties of the MEXICO blade

Section	Span (m)	Chord (m)	Twist ( $^\circ$ )	Profile
1	0.000	0.195	0.000	Cylinder
2	0.020	0.195	0.000	Cylinder
3	0.025	0.090	0.000	Cylinder
4	0.090	0.090	0.000	Cylinder
5	0.165	0.165	8.200	Transition
6	0.240	0.240	16.400	DU91-W2-250
7	0.465	0.207	12.100	DU91-W2-250
8	0.690	0.178	8.300	DU91-W2-250
9	0.815	0.166	7.100	DU91-W2-250
10	0.915	0.158	6.100	Transition
11	1.015	0.150	5.500	RISØ A1-21
12	1.140	0.142	4.800	RISØ A1-21
13	1.265	0.134	4.000	RISØ A1-21
14	1.365	0.129	3.700	Transition
15	1.465	0.123	3.200	NACA64-418
15	1.590	0.116	2.600	NACA64-418
15	1.815	0.102	1.500	NACA64-418
15	1.955	0.092	0.700	NACA64-418
15	1.983	0.082	0.469	NACA64-418
15	2.012	0.056	0.231	NACA64-418
21	2.040	0.011	0.000	NACA64-418

mesh cut a the turbine and vertical centre planes. Previous relevant numerical studies [36, 37] showed that a mesh size equal to  $D/60$  is sufficient to obtain grid independent results for the LES/ALM simulations. The rotor centre is located on the intersection of horizontal and vertical centre planes of the computational domain with a distance  $4D$  from the inlet. The time step is chosen to be  $500^{-1} D/U$  to ensure a good temporal resolution [37, 40]. Each run allows air to get through the domain six times (six flow through times) in order to reach statistically stationary flow conditions. The statistics are then averaged for the last  $\frac{2}{3}$  total run time (four flow through times) to eliminate the effect of initial transience and get statistically stationary mean results. The simulation were run for 5263, 5276 and 5295 core-hours for wind speeds of 10, 15 and  $24 \text{ ms}^{-1}$  respectively. Since resolving the cylinder boundary layer does not really have any influence on the flow field in this study there is no point using a very fine mesh which will increases computational cost. Therefore, a wall model developed based on the Spalding's law [41] is adopted near the solid surface of cylinder representing the nacelle, with the  $y^+$  being approximately 12 for the nearest wall cells.

Table 2: Flow cases

$U_\infty$ (m/s)	$\Omega$ (rpm)	$Re$	TSR	$\theta_p$ ( $^\circ$ )
10	424.5	$3.15 \times 10^6$	10	-2.3
15	424.5	$4.70 \times 10^6$	6.7	-2.3
24	424.5	$7.45 \times 10^6$	4.2	-2.3

For all simulations, because of low turbulence conditions in the experiments, a divergence-free organized perturbations su-

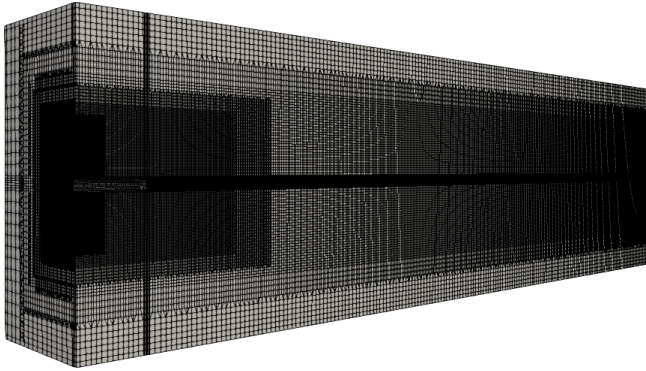


Figure 3: A perspective view of the computational mesh cut at the rotor and vertical centre planes.

perimposed upon a uniform velocity profile are used at the inlet boundary and the zero normal gradient is applied for the velocity at the outlet. At the upstream boundary the normal pressure gradient is set to be zero and a constant pressure is applied on downstream. The four side walls are treated as periodic boundaries. The cylinder is modelled as no slip wall.

### 3. RESULTS AND DISCUSSION

The predicted phase-averaged velocity components in both streamwise and radial traverses, and blade loads are compared with experimental data for three test cases with wind speeds of 10, 15 and 24  $\text{ms}^{-1}$ . For the streamwise traverse, the axial, tangential and radial mean velocity components are presented along two lines in the streamwise direction on the horizontal centre plane at the left side when looking downstream at two radial locations of 0.61 R and 0.82 R from the rotor axis (R is the rotor radius). The experimental data along those two lines in the streamwise direction are available from 2 R upstream to 3 R downstream of the rotor plane. For the radial traverse, the results are presented along a line in the radial direction from 0.523 R to 1.24 R above the rotor axis on the vertical centre plane at a streamwise location of D/15 behind the rotor plane. All velocity components are time-averaged for a particular position of the rotor when one blade is at its top location and normalised by the corresponding approach wind speeds. In terms of blade loads, the predicted mean axial and tangential blade loads are compared against the measurements.

Figure 4 presents iso-surfaces of the second invariant of the velocity-gradient tensor ( $Q$ ), showing instantaneous vortex structures in the flow field coloured by the mean velocity at three wind speeds of 24  $\text{ms}^{-1}$  (top), 15  $\text{ms}^{-1}$  (middle) and 10  $\text{ms}^{-1}$  (bottom). As the figure shows, with decreasing speed of incoming flow which corresponds to increasing the tip speed ratio, the flow behind the turbine experience a higher compression of vortex tubes and the vortex breakdown process and transition to a highly turbulent flow starts sooner. This figure clearly shows that how the complexity of the flow structure behind the turbine increases with increasing the tip speed ratio even

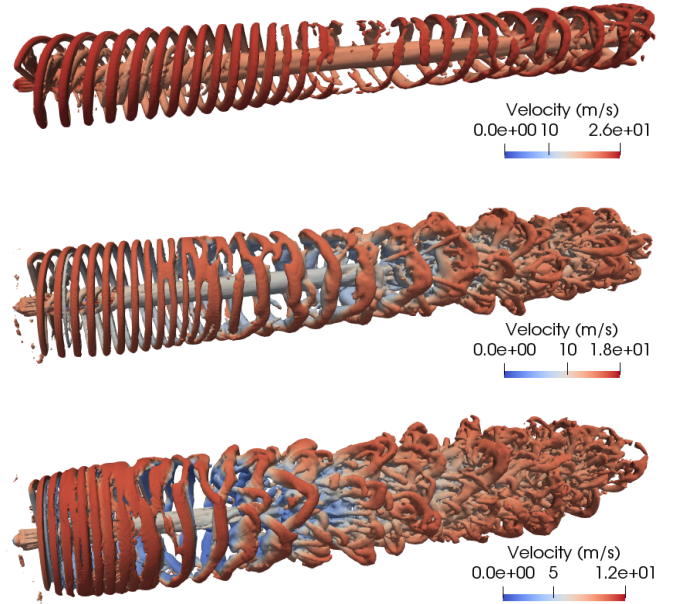


Figure 4: Instantaneous view of vortex structures in the flow field coloured by the mean velocity at wind speeds of 24  $\text{ms}^{-1}$  (top), 15  $\text{ms}^{-1}$  (middle) and 10  $\text{ms}^{-1}$  (bottom).

at lower Reynolds incoming flows with a constant rotational speed.

#### 3.1. Flow field

##### 3.1.1. Streamwise traverse

Figures 5 and 6 present streamwise, tangential and radial phase-averaged velocity components at a wind speed of 24  $\text{ms}^{-1}$  corresponding to  $\text{TSR}=4.16$ , along two lines parallel to the rotor axis located on the horizontal centre plane at the left side when looking downstream at two radial locations of 0.61 R and 0.82 m from the rotor axis. The streamwise, tangential and radial velocity components are presented in the top, middle and bottom frames respectively.

A reasonably good agreement can be seen between the numerical results and experimental data for  $\text{TSR} = 4.16$  at both radial locations. The discrepancies between the predictions and the measurements could be attributed to the simplified computational model in which the tower is ignored and the nacelle is represented by a short cylinder. The oscillations appeared in all velocity components are resulted from the blade vortex shedding. The predictions, particularly for  $v_\theta$ , show clearly that the predicted peak locations agree very well with the measurements. Nevertheless, large discrepancies between the predicted first peak values and the experimental data are clearly observable for  $v_\theta$  and  $v_r$ . One very likely reason for this could be the absence of the turbine blades in the numerical simulations as a result of using the ALM technique, which directly dictate the strength of vortex tubes.

Figures 7 and 8 present three phase-averaged velocity components for the case with a wind speed of 15  $\text{ms}^{-1}$  corresponding to  $\text{TSR}= 6.7$ , along two lines parallel to the rotor axis at the same locations as in Figure 5. It can be seen from the

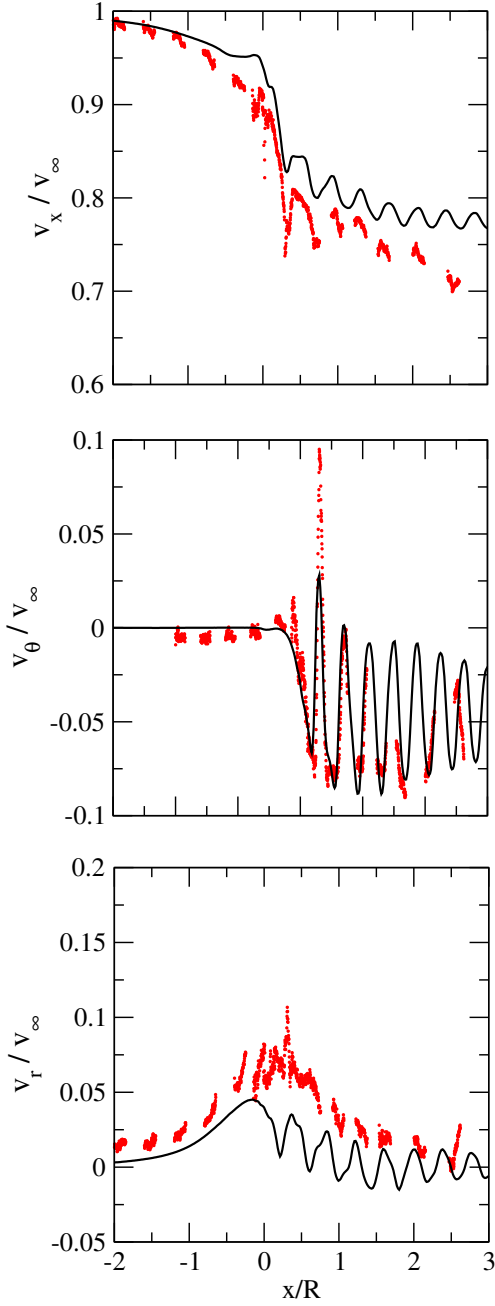


Figure 5: Axial (top), tangential (middle) and radial (bottom) velocity components along a line in the streamwise direction on the horizontal centre plane at the left side of the rotor axis when looking downstream at  $r = 0.61 R$  from it for a wind speed of  $24 \text{ ms}^{-1}$ ; red line: Exp., black lines: CFD.

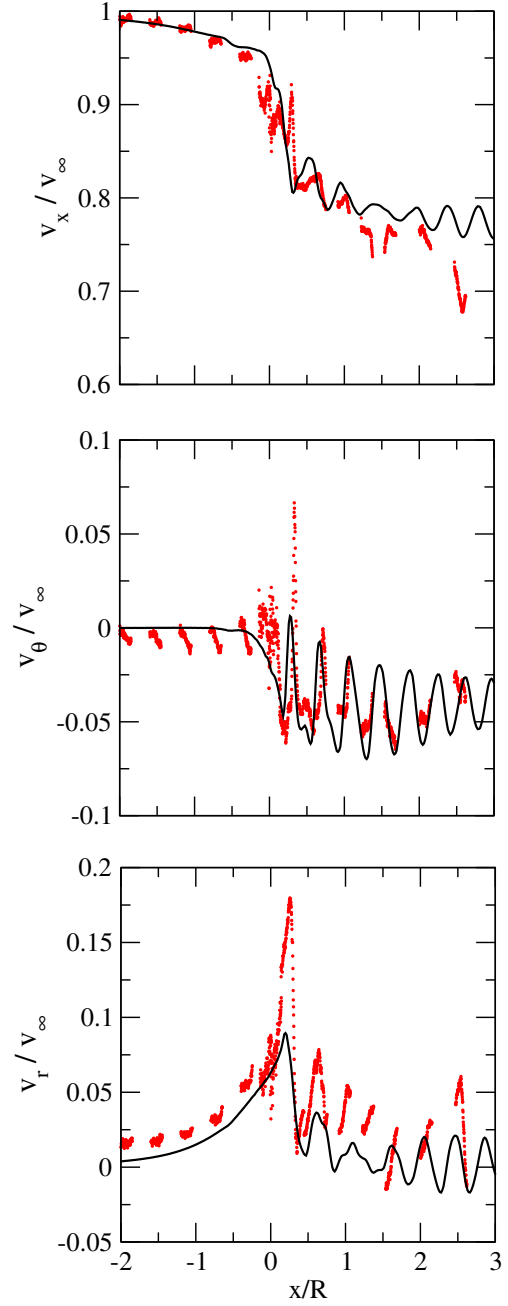


Figure 6: Axial (top), tangential (middle) and radial (bottom) velocity components along a line in the streamwise direction on the horizontal centre plane at the left side of the rotor axis when looking downstream at  $r = 0.82 R$  from it for a wind speed of  $24 \text{ ms}^{-1}$ ; red lines: Exp., black lines: CFD.

comparison at the top frames that at both locations  $0.61 R$  and  $0.82 R$ , the streamwise velocity component ( $v_x$ ) is over-predicted. This is consistent with all numerical simulations reported in "Analysis of MEXICO wind tunnel measurements, Final report" [2]. Under this flow condition, the experimental data for  $v_x$  at location  $0.61 R$  show some small oscillations which is not clearly observable in the predicted  $v_x$ . As reported by Schepers *et al.* [2], contrary to the previous case ( $\text{TSR} = 4.16$ ), under this flow condition ( $\text{TSR} = 6.7$ ) the oscillations appeared in the experimental data at  $0.61 R$  (Figure 3 -

top frame) were not due to vortex shedding but caused by the profile transition along the blade span which would not be captured by the numerical simulations.

The comparison between the predicted tangential velocity components and experimental data are presented in the middle frames. Under this flow condition, the agreements are not as good as those in the previous case ( $\text{TSR} = 4.16$ ) and the predicted velocity oscillations at both radial locations  $0.61 R$  and  $0.82 R$  are much smaller than the experimental ones and decay very rapidly. Similar results have been reported by Schep-

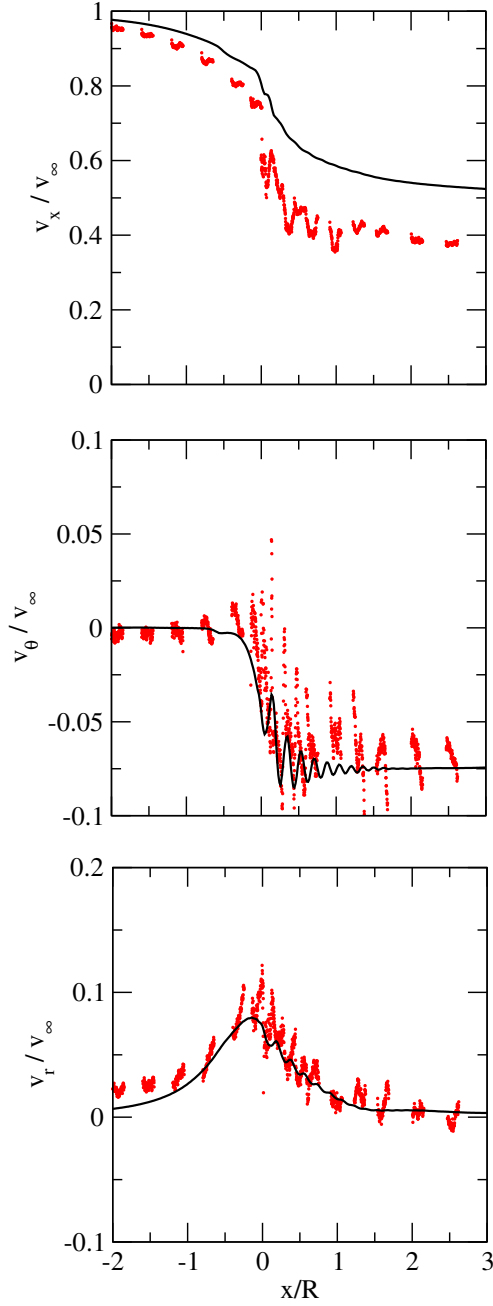


Figure 7: Axial (top), tangential (middle) and radial (bottom) velocity components at the location explained in Figure 5 for a wind speed of  $15 \text{ ms}^{-1}$ ; red lines: Exp., black lines: CFD.

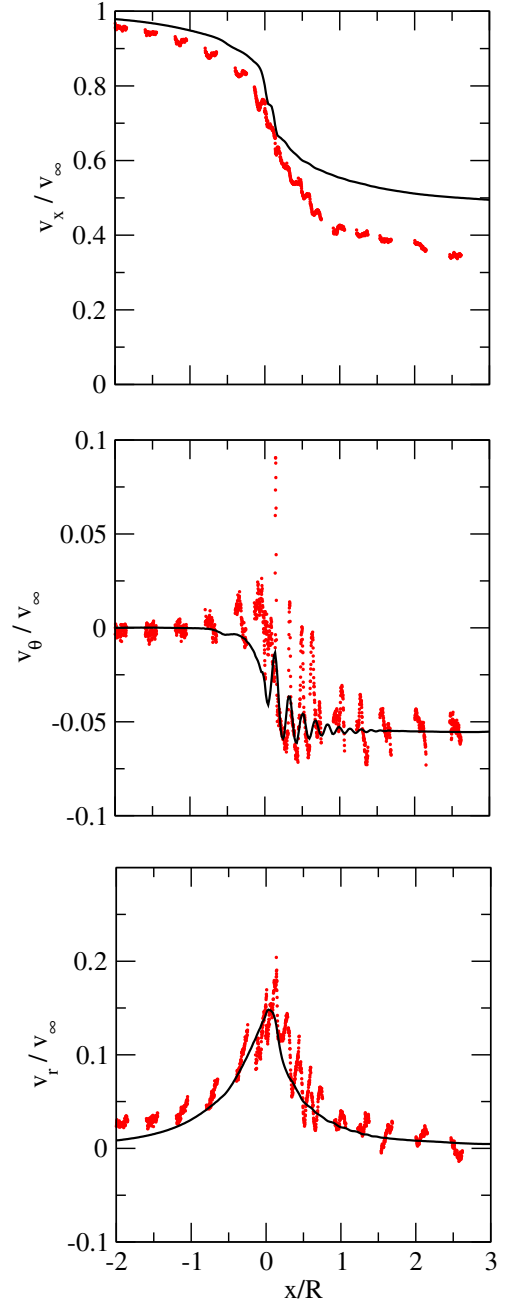


Figure 8: Axial (top), tangential (middle) and radial (bottom) velocity components at the location explained in Figure 6 for a wind speed of  $15 \text{ ms}^{-1}$ ; red lines: Exp., black lines: CFD.

ers *et al.* [2] and they attributed this to the overly dissipative nature of the used turbulence models. However, a previous numerical study of tidal turbines by the authors [42] demonstrated that in the nearwake before the transition, the turbulence level is usually comparable with that in the upstream flow and is just a little higher because of the mechanical turbulence generated by the blade boundary layer and vibration. Therefore, the reason reported by Schepers *et al.* [2], i.e., the overly dissipative nature of the used turbulence models, may not be the main reason for the discrepancies. As can be seen in Figure 4, the complexity of the flow behind the turbine increases with

increasing the tip speed ratio even at lower Reynolds approaching flows. In this study and numerical simulations reported by Schepers *et al.* [2], the same mesh has been used for all wind speeds and considering the higher complexity of the flow at higher TSRs a mesh resolution sufficient for a lower TSR case (4.16) may not be sufficient for a higher TSR case (6.7). Furthermore, the timesteps ( $\Delta t$ ) have been determined based on the upstream wind speeds/Reynolds numbers ( $Re$ ), leading to a smaller  $\Delta t$  for the higher wind speed cases (lower TSRs) and larger  $\Delta t$  for the lower wind speeds (higher TSRs). Using a larger  $\Delta t$  in the numerical simulations leads to larger azimuthal

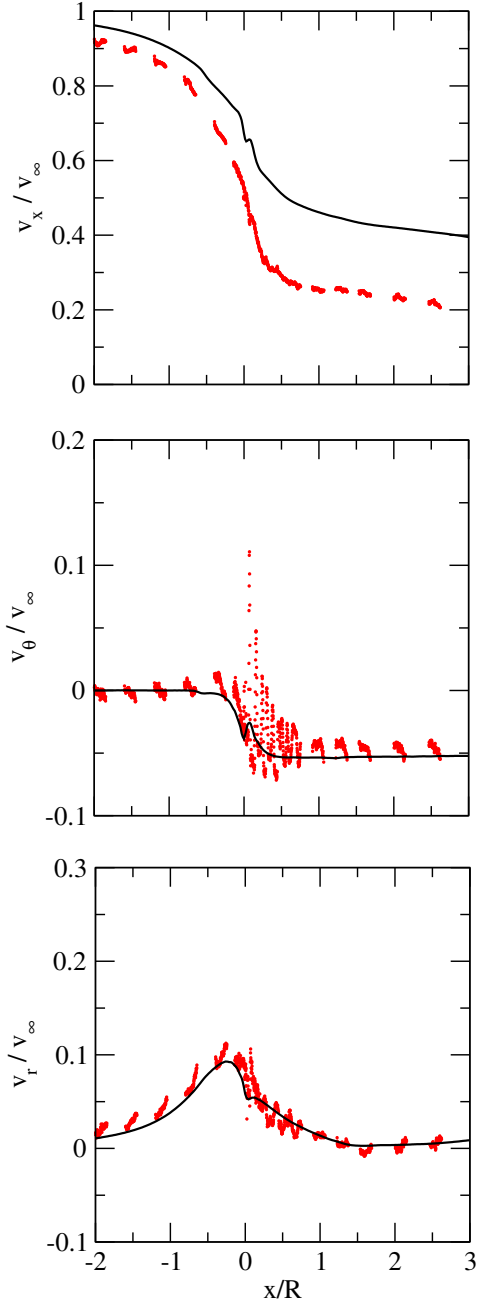


Figure 9: Axial (top), tangential (middle) and radial (bottom) velocity components at the location explained in Figure 5 for a wind speed of  $10 \text{ ms}^{-1}$ ; red lines: Exp., black lines: CFD.

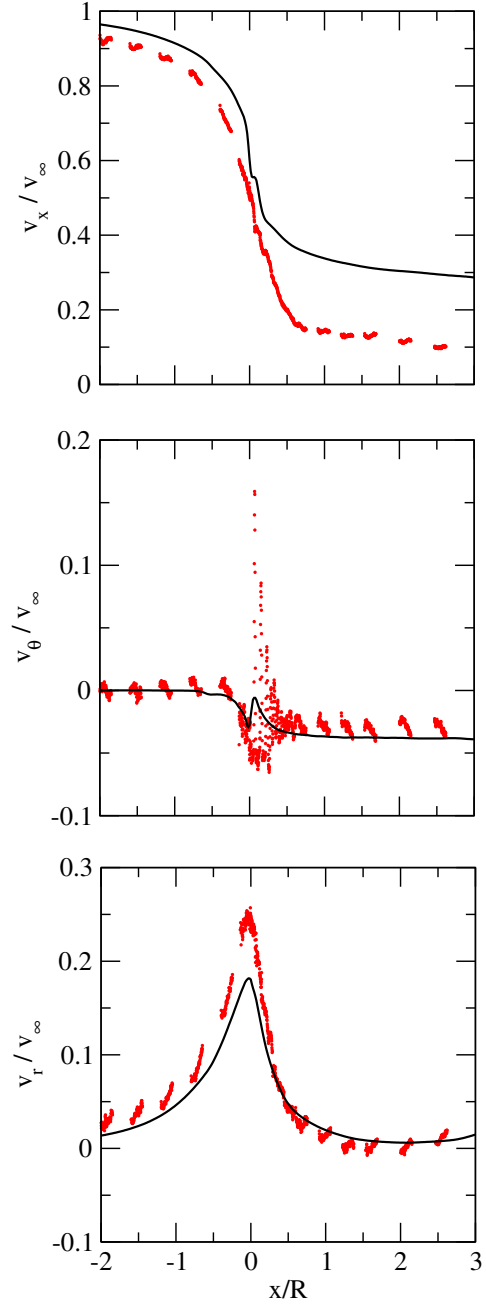


Figure 10: Axial (top), tangential (middle) and radial (bottom) velocity components at the location explained in Figure 6 for a wind speed of  $10 \text{ ms}^{-1}$ ; red lines: Exp., black lines: CFD.

angle at each timestep, resulting in less accurate results. Therefore, the authors believe that using a  $\Delta t$  determined based on the rotational speed rather than upstream  $\text{Re}$  should be considered as possible solutions to improve the accuracy of predictions. Further studies are needed to systematically investigate the effects of smaller  $\Delta t$ , finer mesh and different SGS models on the accuracy of the numerical results. Bottom frames in Figures 7 and 8 present the comparison between the experimental and numerical results for radial velocity components. The comparison shows that the predicted results agree well with the experimental data at both locations.

Figures 9 and 10 present the comparison between the predicted velocity components and experimental data at a wind speed of  $10 \text{ ms}^{-1}$  corresponding to  $\text{TSR} = 10$  along the same two lines in the streamwise direction at the same two radial locations as those in previous Figures. The comparisons between the predicted streamwise and radial velocity components and the corresponding experimental data under this flow condition are similar to those for the case at a wind speed of  $15 \text{ ms}^{-1}$ , with slightly larger discrepancies. However, for tangential velocity components shown in the middle frames of the figures, the comparison is much worse than that for the case at a wind

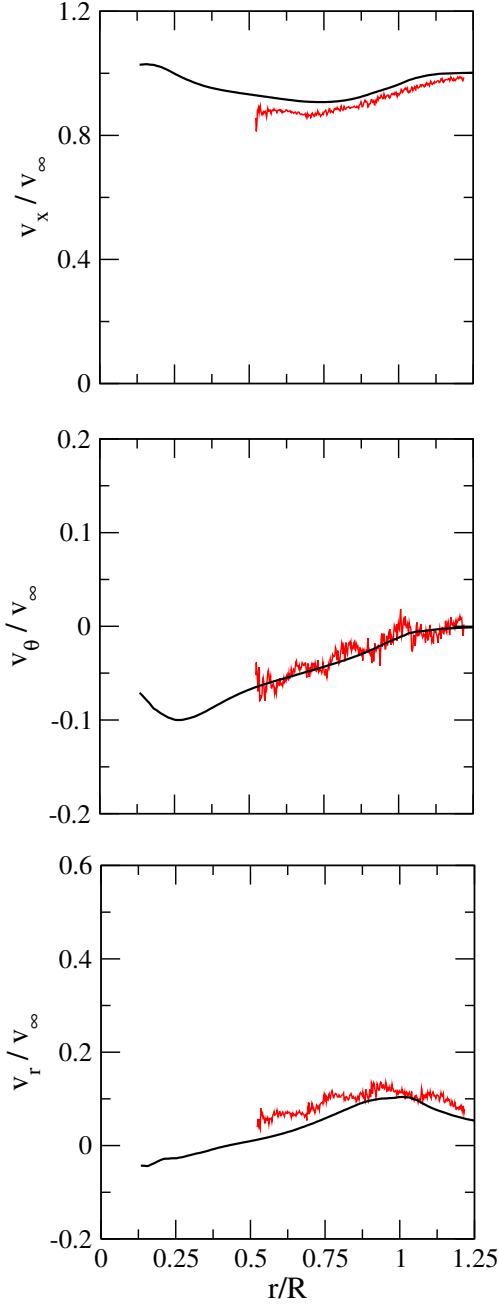


Figure 11: Axial (top), tangential (middle) and radial (bottom) velocity components along a line in the radial direction at the vertical centre plane at a location  $D/15$  behind the turbine for a wind speeds of  $24\text{ ms}^{-1}$ ; red lines: Exp., black lines: CFD.

speed of  $15\text{ ms}^{-1}$  since the oscillations shown in the experimental data are not well captured at all. Similar to the case with  $\text{TSR}=6.7$ , these results are consistent with those obtained using different numerical codes and presented in the report by Schepers *et al.* [2]. All possible reasons for the discrepancies are the same as those given above for the case at a wind speed of  $15\text{ ms}^{-1}$  but under this case at a wind speed of  $10\text{ ms}^{-1}$ , because of the highest complexity of the downstream flow and using the largest time step among the three cases studied, these are the worst predictions among the three cases.

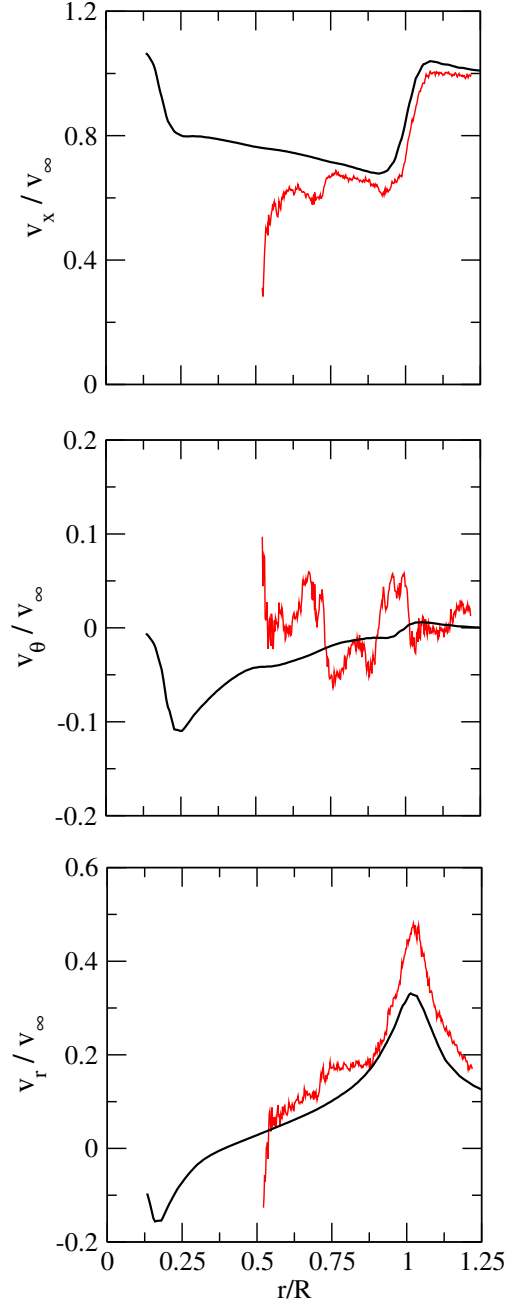


Figure 12: Axial (top), tangential (middle) and radial (bottom) velocity components at a location explained in Figures 11 for a wind speeds of  $15\text{ ms}^{-1}$ ; red lines: Exp., black lines: CFD.

### 3.1.2. Radial traverse

The predicted axial, tangential and radial phase-averaged velocity profiles at a wind speed of  $24\text{ ms}^{-1}$  ( $\text{TSR}=4.16$ ) along a line in the radial direction on the vertical centre plane at a distance  $D/15$  behind the rotor plane are compared with the experimental data in Figure 11. In this figure, radial positions have been normalised by the rotor radius. The comparison shows that a very good agreement between the predictions and measurements has been obtained under this low TSR operating condition.

Figure 12 presents comparisons between the predicted phase-

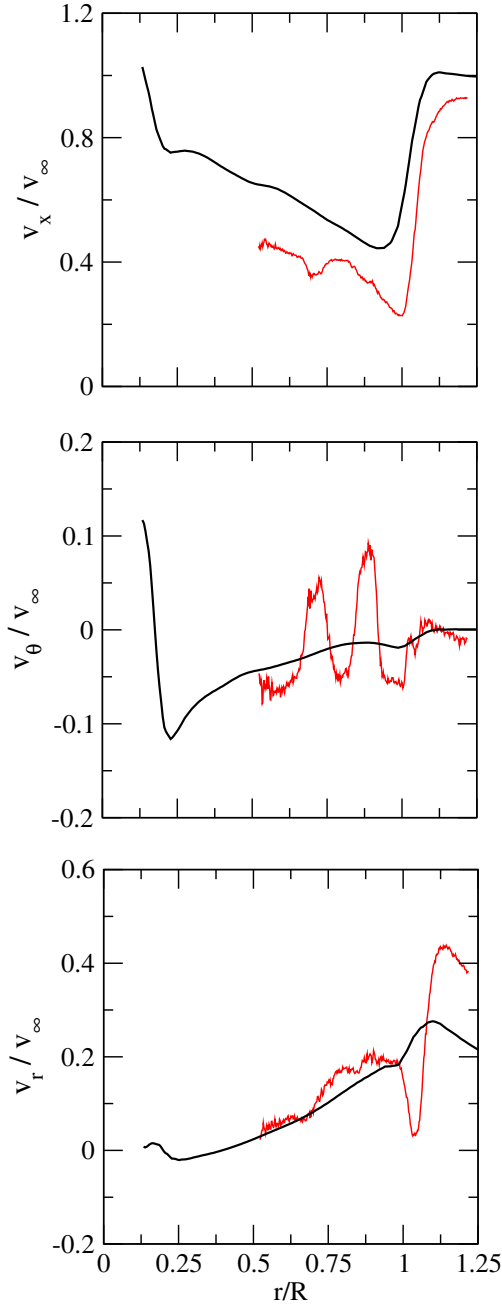


Figure 13: Axial (top), tangential (middle) and radial (bottom) velocity components at a location explained in Figures 11 for a wind speeds of  $10 \text{ ms}^{-1}$ ; red lines: Exp., black lines: CFD.

averaged velocity profiles and experimental data at a wind speed  $15 \text{ ms}^{-1}$  ( $\text{TSR} = 6.7$ ) at the same location as in Figure 11. The measurements show a dip in axial (top frame) and radial (bottom frame) velocity components around radial position  $0.52R$ . As discussed in the report [2], it is believed that this dip is related to the transition in the airfoil geometry along the blade span, which could not be captured in the numerical simulations presented here because the blade geometry is not resolved but modelled by the ALM technique. Apart from this dip, it can be seen that the predicted  $v_x$  and  $v_r$  agree well with the measurements. Contrary to the axial and radial velocity components,

the predicted tangential velocity shows large deviations from experimental data. As shown in the middle frame of Figure 12, the measured tangential velocity shows sharp variations along the radial direction apart from those induced by tip vortices. As addressed in the same report [2], these humps are caused by slicing through the viscous blade wake which does not featured a straight line in radial direction due to the varying convection speed along the blade span and have not been predicted properly by any of the CFD codes used in it. Nevertheless, it is worth pointing out that the values of  $v_\theta$  are very small, which could be very sensitive to many factors and hence is very hard to predict accurately. As discussed in Section 3.1.1, using a finer mesh and smaller  $\Delta t$  under this flow condition ( $\text{TSR} = 6.7$ ) may improve the accuracy of the numerical results and further studies are required to evaluate this.

The comparisons between the predicted velocity profiles and experimental data at the same location at a wind speed of  $10 \text{ ms}^{-1}$  ( $\text{TSR} = 10$ ) are shown in Figure 13. It can be seen from the top frame of the figure that a reasonably good agreement has been obtained for the axial velocity component. The predicted radial velocity agrees well with the experimental data below blade tip ( $r/R < 1$ ) but above the blade tip region ( $r/R > 1$ ) a sharp reduction followed by a rapid increase shown in the measurements are not captured by the numerical simulations. As discussed above, possible reason for this could be the coarse mesh near the tip region and  $\Delta t$  being too large under this high TSR condition. Further studies are needed to clarify this. For the tangential velocity, similar to the case above with a wind speed of  $15 \text{ ms}^{-1}$ , large discrepancies exist between the predictions and the measurements due to the same reasons given above.

### 3.2. Blade loading

The comparisons between the predicted axial/tangential mean blade loads and experimental data at wind speeds of 10, 15 and  $24 \text{ ms}^{-1}$  are shown at the top, middle and bottom frames of Figure 14 respectively. It can be seen from the top and middle frames that a very good agreement between the predictions and experimental data has been obtained for the cases with wind speeds of  $10 \text{ ms}^{-1}$  and  $15 \text{ ms}^{-1}$ . However, at the wind speed of  $24 \text{ ms}^{-1}$  the agreement is not so good, especially for the axial force. This is most likely due to the fact that the measurements show flow separation [2] at the wind speed of  $24 \text{ ms}^{-1}$ , which cannot be captured by the current numerical simulations since the blade geometry is not resolved but modelled using the ALM method.

Plots in the bottom frame show overpredictions of axial loads at 82% and 92% span for a wind speed of  $24 \text{ ms}^{-1}$ . Considering the flow separation in this flow condition suggests that the overprediction of axial loads can be related to a delay in predicting separation point compared to the experiment. In the same way, underprediction of axial loads at the inner part of the blade can be attributed to an underprediction of stall delay in this flow condition. Comparing the predicted and measured tangential forces show a similar behaviour and can be demonstrated in a similar way. This indicates that care should be taken when applying

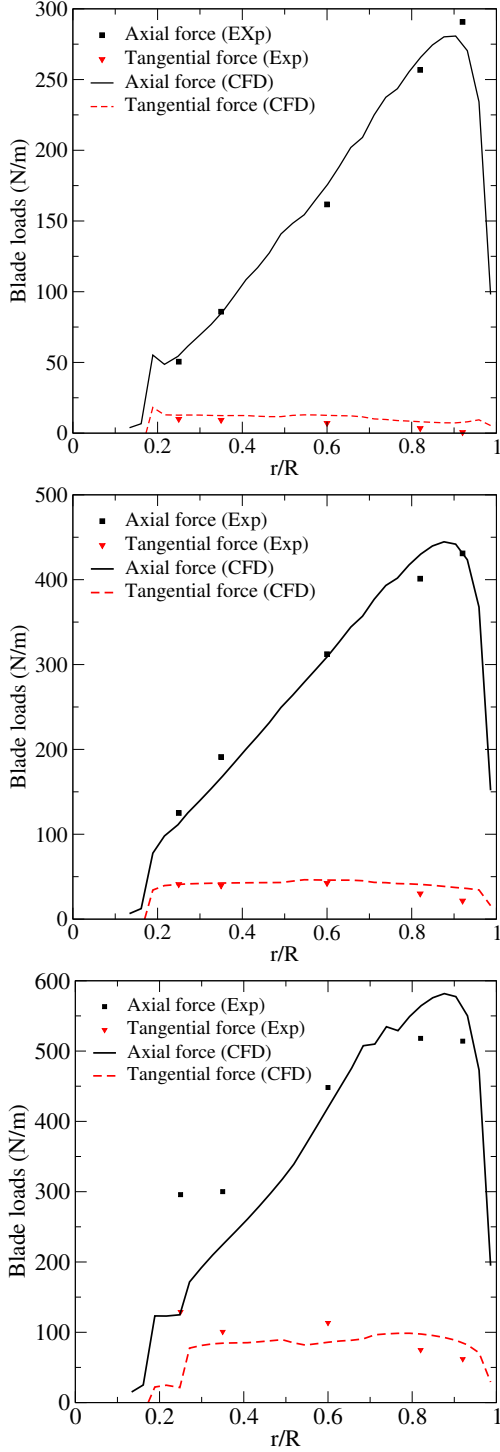


Figure 14: Axial and tangential forces on the rotor blades at wind speeds of  $10 \text{ ms}^{-1}$  (top),  $15 \text{ ms}^{-1}$  (middle) and  $24 \text{ ms}^{-1}$  (bottom).

ALM method to model turbine blades on which flow separation may occur.

### 3.3. Thrust and torque loads frequency analysis

Experimental studies [21, 22, 23, 24] have shown a coupling between the instantaneous turbine response and turbulence in

the incoming flow. To further investigate this coupling, the predicted spectral density of thrust, power and approaching flow velocity components at three wind speeds are presented in Figures 15- 20. The frequency in the figures is normalised by the turbine rotational frequency,  $f_0$ . At each wind speed, power spectra of three velocity components at the rotor plane near the hub and one diameter upstream at the rotor height are presented. The thrust and power coefficients are defined respectively as follows:

$$C_T = \frac{T}{\frac{1}{2}\rho A_r V_\infty^2} \quad \text{and} \quad C_P = \frac{Q\omega}{\frac{1}{2}\rho A_r V_\infty^3} \quad (3)$$

where  $\rho$  is density,  $T$ ,  $Q$  and  $\omega$  denote the rotor thrust, torque and rotational speed respectively and  $A_r$  presents the rotor area. As mentioned above, velocity components are normalised by the corresponding wind speed for each case.

Figure 15 shows the comparison between PSD of the power coefficient and PSD of three velocity components at two axial locations, the rotor plane and 1 D upstream of it, at a wind speed of  $15 \text{ ms}^{-1}$  (TSR= 6.7). The streamwise velocity PSD at the location 1 D upstream of the rotor plane (red line) is quite similar to the power coefficient PSD (blue line) for frequencies below  $1.5 f_0$  as shown in the top frame of the figure. However, for frequencies higher than that ( $f > 1.5 f_0$ ) their trends change completely as the power coefficient PSD shows large peaks at  $3f_0$  and its harmonics at  $6f_0$ ,  $9f_0$ ,  $12f_0$  etc. whereas the streamwise velocity PSD shows a monotonously decreasing behaviour without any peaks. This clearly indicates that there exists a coupling between the instantaneous turbine power and the incoming turbulent flow field for frequencies below  $1.5 f_0$  but this coupling does not exist for frequencies above that frequency. This is consistent with the previous study by Payne *et al.* [24]. It is very different for the streamwise velocity PSD at the rotor plane (green line) which is quite similar to the power coefficient PSD for all frequencies, with the peaks at exactly the same frequencies. This suggests that a coupling between the instantaneous turbine power and the velocity field at the rotor plane exist for all frequencies. As already addressed by the authors [42], the nature of velocity fluctuations at the rotor plane and shortly downstream differs from that of upstream due to the deterministic velocity fluctuations (DVF) generated by the turbine rotation. This difference leads to the decoupling shown in the figure between the PSD of axial velocity components at the rotor plane and 1 D upstream of it at  $f > 1.5f_0$ . The coupling seen between the PSDs of the axial velocity component at the rotor plane and the power coefficient suggests that the pattern of former dictates the latter one.

PSD obtained from the radial and tangential velocity components are very similar to the axial velocity PSD, as shown in the middle and bottom frames of the figure, confirming the above findings from comparison between the axial velocity PSD and PSD of the power coefficient.

Figure 16 presents the comparison between PSD of the thrust coefficient and PSDs of three velocity components at the same axial locations as in Figure 15, and at the same wind speed of  $15 \text{ ms}^{-1}$ . It can be seen clearly that the behaviour of thrust PSD is more or less the same as that of the power PSD and hence it

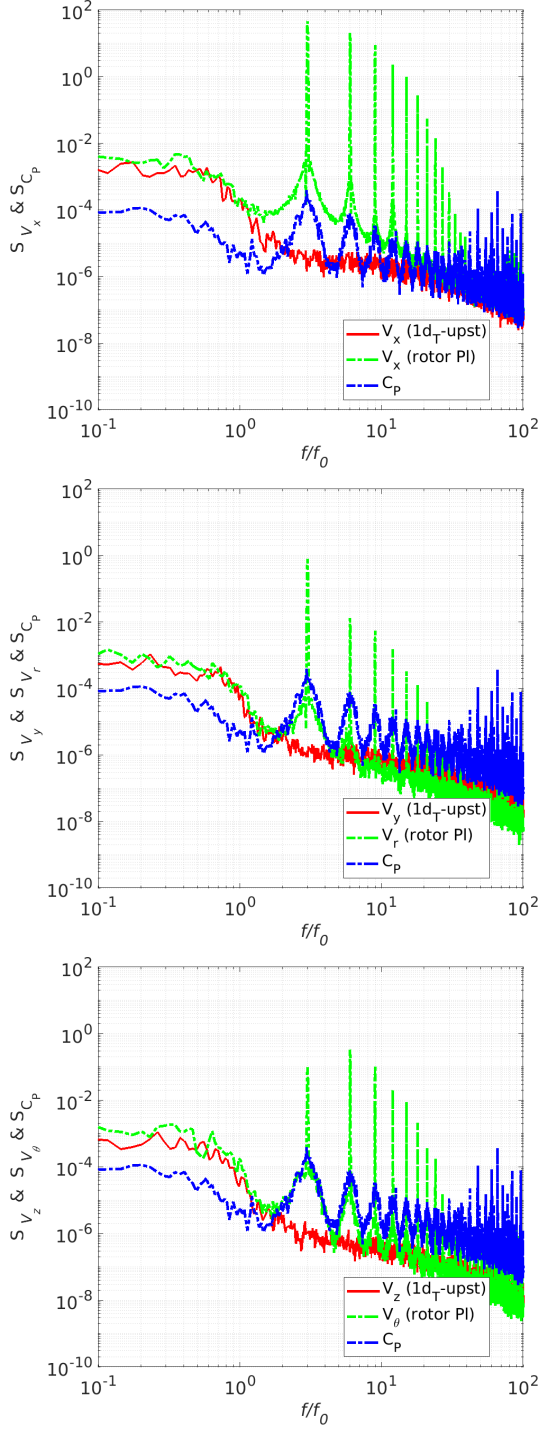


Figure 15: Power spectra of  $C_p$  and normalised axial, tangential and radial velocity components at top, middle and bottom frames respectively at 1 D up-stream and rotor planes at a wind speed of  $15 \text{ ms}^{-1}$ .

can be said that the instantaneous responses of thrust and power to upstream flow are similar.

At a wind speed of  $10 \text{ ms}^{-1}$  corresponding to high TSR= 10, the velocity PSD at the same two axial locations, the rotor plane and 1 D upstream of that, are plotted together with PSDs of the power and thrust coefficients in Figures 17 and 18. It is clearly observable that both the velocity PSDs and PSDs of

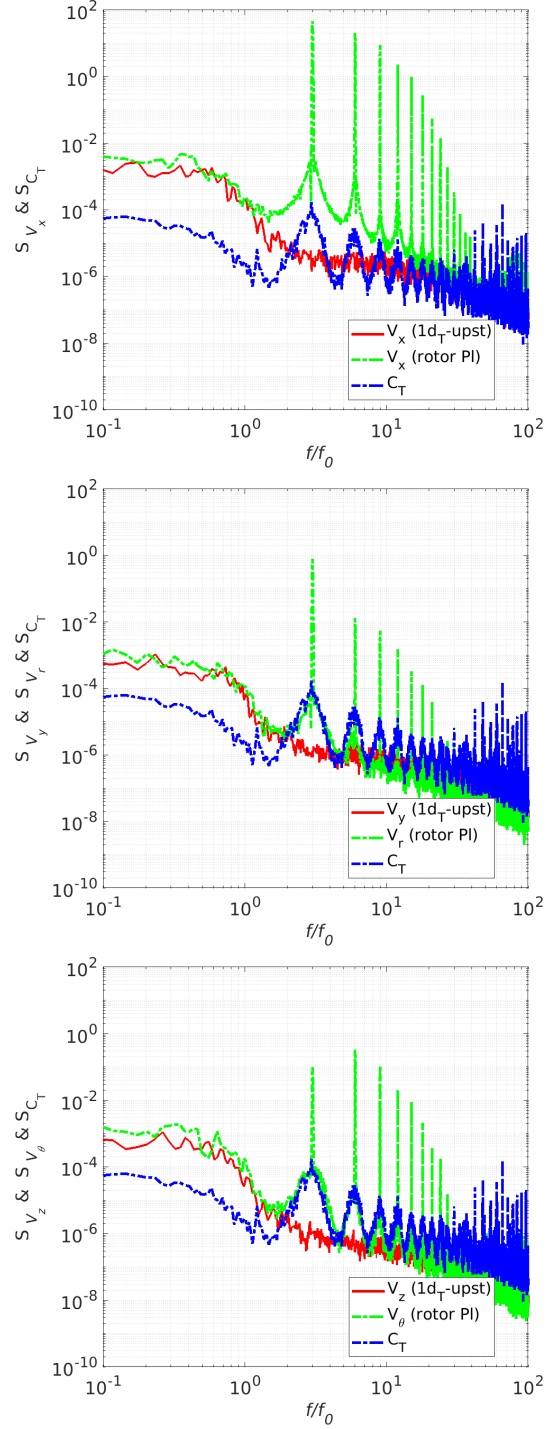


Figure 16: Power spectra of  $C_t$  and normalised axial, tangential and radial velocity components at top, middle and bottom frames respectively at 1 D up-stream and rotor planes at a wind speed of  $15 \text{ ms}^{-1}$ .

the power/thrust coefficients in this case are very similar to those presented in the previous case (wind speed of  $15 \text{ ms}^{-1}$ , TSR= 6.7) apart from two differences. Firstly, in this case, the decoupling between PSDs of power/thrust and the velocity PSD at 1 D upstream of the rotor plane start at about  $0.7f_0$  rather than  $1.5f_0$  seen in the previous case. Secondly, the coupling between the velocity PSD at the rotor plane and PSDs of power/thrust is

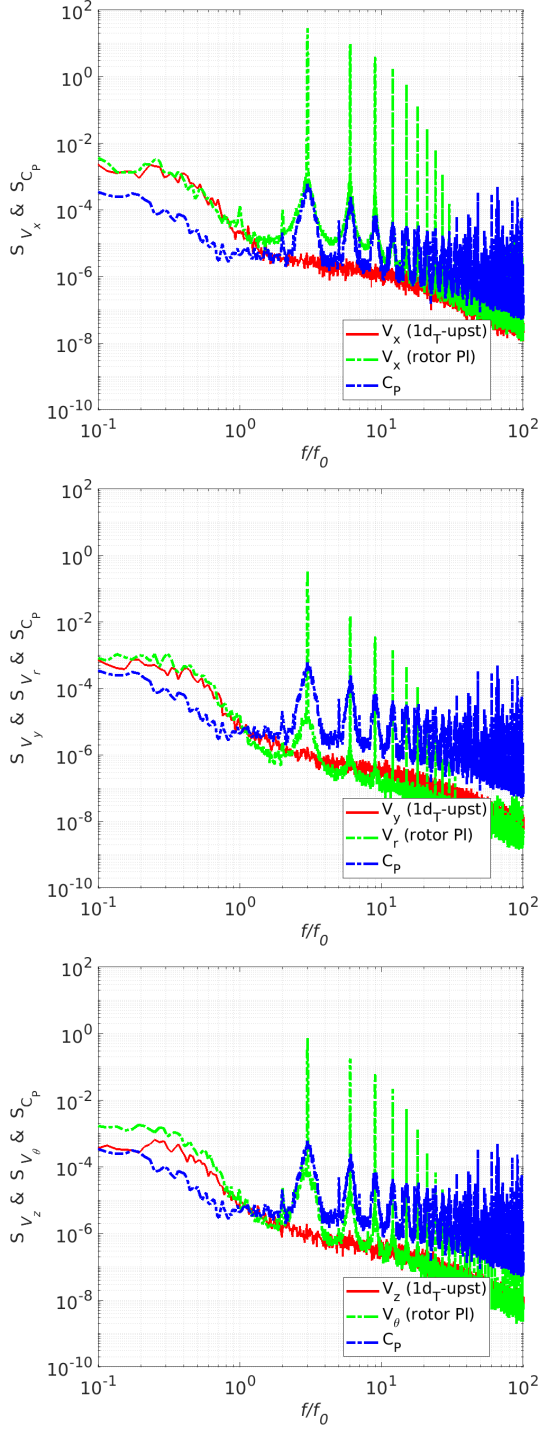


Figure 17: Power spectra of  $C_p$  and normalised axial, tangential and radial velocity components at top, middle and bottom frames respectively at 1D up-stream and rotor planes at a wind speed of  $10 \text{ ms}^{-1}$ .

a little affected at the frequency range of  $0.7f_0 - 2f_0$  particularly for tangential and radial velocity components where the PSDs of power/thrust show a more or less constant behaviour. These characteristics may be related to the high TSR of this case and requires further studies to clarify them. Nevertheless, despite the above two differences, the same conclusion can be drawn regarding the coupling between the instantaneous turbine re-

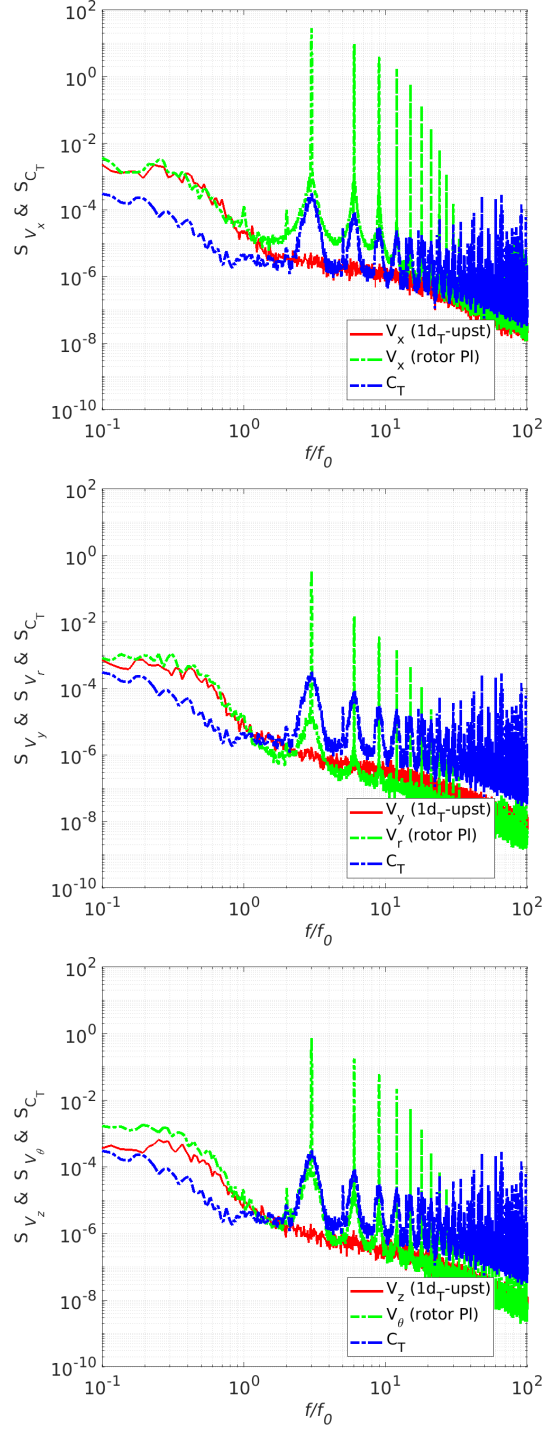


Figure 18: Power spectra of  $C_T$  and normalised axial, tangential and radial velocity components at top, middle and bottom frames respectively at 1D up-stream and rotor planes at a wind speed of  $10 \text{ ms}^{-1}$ .

sponse and turbulent flow fields, i.e., a coupling between the instantaneous turbine power/thrust and the incoming turbulent flow field exists only for frequencies below a critical frequency close to the turbine rotational frequency whereas the instantaneous turbine power/thrust is coupled with the turbulent flow field at the rotor plane for all frequencies.

Figures 19 and 20 present PSDs of the power/thrust coef-

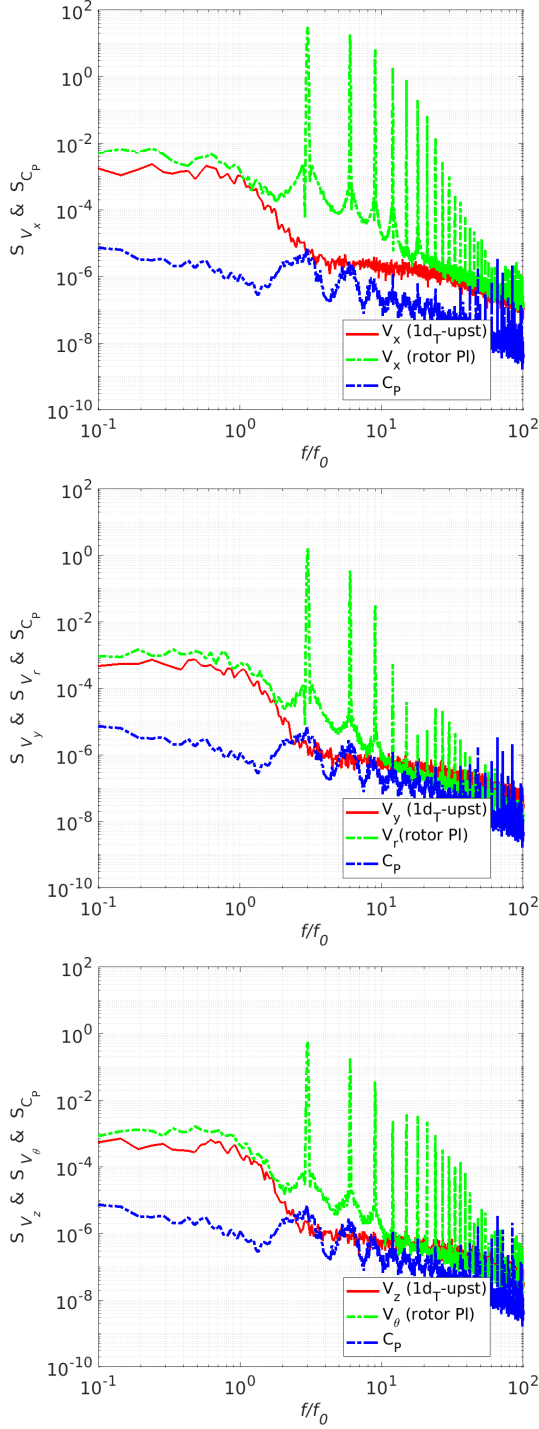


Figure 19: Power spectra of  $C_p$  and normalised axial, tangential and radial velocity components at top, middle and bottom frames respectively at 1 D upstream and rotor planes at a wind speed of  $24 \text{ ms}^{-1}$ .

ficients together with the velocity PSDs at the same axial locations as in previous figures (1 D upstream of the rotor plane and the rotor plane), at a wind speed of  $24 \text{ ms}^{-1}$  ( $\text{TSR} = 4.16$ ). The velocity PSDs in this case are very similar to the velocity PSDs in the other two cases ( $\text{TSR} = 10$  and  $= 6.7$ ) and the power coefficient PSD is also very similar to that in the case with  $\text{TSR} = 6.7$ . However, the thrust coefficient PSD shows a

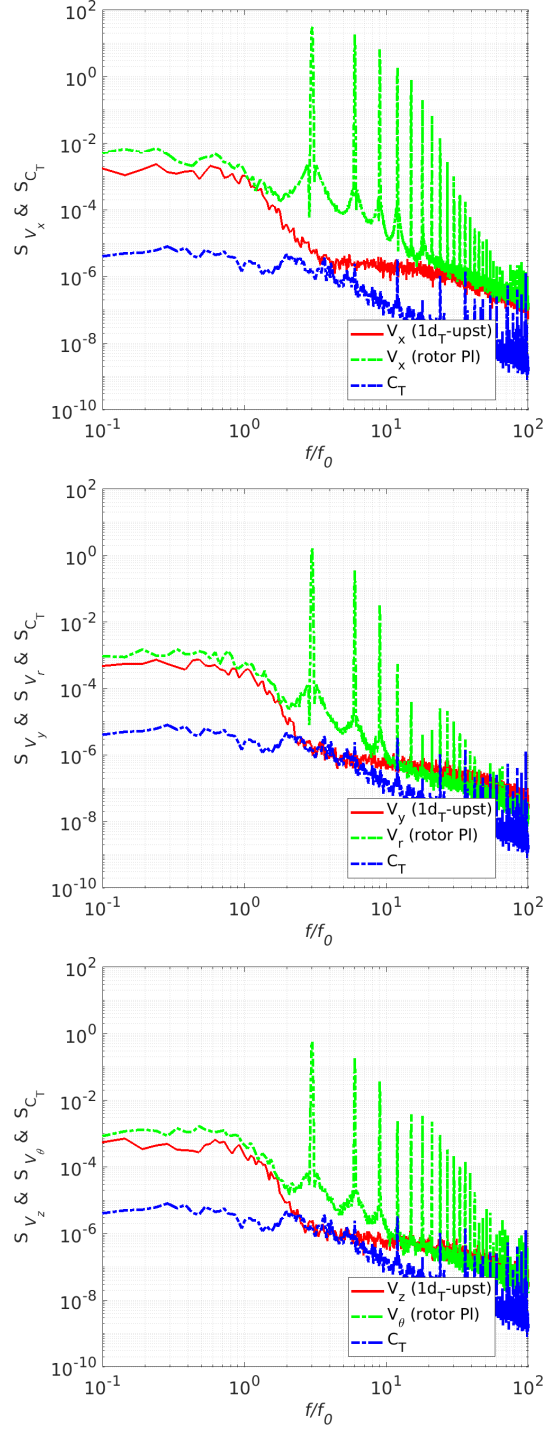


Figure 20: Power spectra of  $C_T$  and normalised axial, tangential and radial velocity components at top, middle and bottom frames respectively at 1 D upstream and rotor planes at a wind speed of  $24 \text{ ms}^{-1}$ .

different behaviour in this flow condition and especially that all those sharp peaks at  $3f_0$  and its harmonics at  $6f_0$ ,  $9f_0$ ,  $12f_0$  etc. are not present at all. One plausible explanation is that the flow separation under this condition (wind speed of  $24 \text{ ms}^{-1}$ ) could not be captured by the numerical simulations since the blade geometry is not resolved but modelled by the ALM method, leading to the inaccurate predictions for the axial force as shown

in the bottom frame of Figure 14. Nevertheless, the tangential force is still reasonably well predicted under the same condition (wind speed of  $24 \text{ ms}^{-1}$ ) and hence the power coefficient PSD shows a behaviour comparable to those in the other two cases.

It is clear from the above discussions that PSD of the power and thrust coefficients has strong similarity to the velocity PSD at the rotor plane. This has important implication in that when investigating the effects of upstream flow characteristics such as turbulence intensities/scales on the instantaneous turbine power and loads, one can study the effects of upstream flow on the instantaneous flow fields at the rotor plane or shortly behind it which can provide useful information for understanding the effects of upstream turbulence on the instantaneous turbine behaviours because measuring the instantaneous turbine power/loads is extremely difficult, often not feasible.

#### 4. Conclusion

A horizontal-axis wind turbine has been numerically simulated using the hybrid LES/ALM technique for different tip speed ratios at high Reynolds numbers. The predicted phase-averaged velocity profiles along both the axial and radial directions agree well with the experimental data. A good agreement has also been obtained between the predicted axial and tangential forces on the turbine blades and the measurements apart from the case at the highest wind speed of  $24 \text{ ms}^{-1}$  (corresponding to the lowest TSR) where flow separation occurs which cannot be captured by the hybrid numerical approach used. Furthermore, it has been found the tangential velocity component is quite small and hence difficult to be predicted accurately, particularly for the cases at high tip speed ratios of 6.7 and 10 (corresponding to speed winds of  $15 \text{ ms}^{-1}$  and  $10 \text{ ms}^{-1}$ ).

The spectral analysis in the present study confirms that a coupling between the instantaneous turbine thrust/power and the upstream turbulence (one rotor diameter upstream of the turbine) exists for frequencies below a critical frequency close to the turbine rotational frequency. The present study also reveals for the first time that PSD of the turbine thrust/power and the velocity PSD at the rotor plane are very similar for all frequencies, which means a strong coupling between the instantaneous turbine power/thrust and the velocity field at the rotor plane. Those findings in the present study clearly suggest that the velocity PSD at the rotor plane or shortly behind it can provide very useful information for understanding the instantaneous turbine loads which are extremely difficult to measure directly but very important for the turbine operational life. Furthermore, for frequencies below a critical frequency close to the turbine rotational frequency, the instantaneous turbine response to the upstream turbulence could be obtained by analysing the velocity PSD at the rotor plane location or shortly behind it since PSD of the turbine power/thrust is very similar to the velocity PSD.

#### CRedit author statement

**Mohammad Ahmadi:** Conceptualization, Methodology, Software, Resources, Validation, Formal analysis, Investiga-

tion, Data curation, Writing- Original draft preparation, Visualization, Writing- Review & Editing. **Zhiyin Yang:** Writing - Review & Editing, Supervision, Project administration.

#### Acknowledgements

The authors would like to thank The School of Mechanical Engineering and the Built Environment for kindly providing us with HPC resources making this project possible. The data used have been supplied by the consortium which carried out the EU FP5 project Mexico: 'Model rotor EXperiments In COntrolled conditions.

#### References

- [1] P. Milan, M. Wächter, J. Peinke, Turbulent Character of Wind Energy, *Phys. Rev. Lett.* 110 (2013) 138701.
- [2] J. Schepers, K. Boorsma, T. Cho, S. Gomez-Iradi, P. Schaffarczyk, A. Jeromin, W. Z. Shen, T. Lutz, K. Meister, B. Stoevesandt, S. Schreck, D. Micallef, R. Pereira, T. Sant, H. Aagaard Madsen, N. N. Sørensen, Analysis of Mexico wind tunnel measurements, Final report of IEA Task 29, Mexnext (Phase 1), Tech. rep., ECN, ECN-E-12-004 (2012).
- [3] J. Schepers, K. Boorsma, S. Gomez-Iradi, P. Schaffarczyk, H. Madsen, N. Sørensen, W. Shen, T. Lutz, C. Schultz, I. Herraiez, S. Schreck, Final report of IEA Wind Task 29: Mexnext (Phase 2), Tech. rep., ECN, ECN-E-14-060 (2014).
- [4] K. Boorsma, J. Schepers, S. Gomez-Iradi, I. Herraiez, T. Lutz, P. Weihing, L. Oggiano, G. Pirrung, H. A. Madsen, W. Z. Shen, H. Rahimi, P. Schaffarczyk, Final report of IEA Wind Task 29: Mexnext (Phase 3), Tech. rep., ECN, ECN-E-18-003 (2018).
- [5] J. Herp, U. V. Poulsen, M. Greiner, Wind farm power optimization including flow variability, *Renew. Energy* 81 (2015) 173–181.
- [6] J. Thé, H. Yu, A critical review on the simulations of wind turbine aerodynamics focusing on hybrid RANS-LES methods, *Energy* 138 (2017) 257–289.
- [7] R. Storey, J. Cater, S. Norris, Large eddy simulation of turbine loading and performance in a wind farm, *Renew. Energy* 95 (2016) 31–42.
- [8] P. M. O. Gebraad, F. W. Teeuwisse, J. W. van Wingerden, P. A. Fleming, S. D. Ruben, J. R. Marden, L. Y. Pao, Wind plant power optimization through yaw control using a parametric model for wake effects—a CFD simulation study, *Wind Energy* 19 (2016) 95–114.
- [9] R. J. A. M. Stevens, C. Meneveau, Flow Structure and Turbulence in Wind Farms, *Annu. Rev. Fluid Mech* 49 (2017) 311–39.
- [10] P. Moriarty, A. Hansen, AeroDyn Theory Manual, Tech. rep., National Renewable Energy Laboratory, nREL/TP-500-36881 (2005).
- [11] E. Smilden, A. Sørensen, L. Eliassen, Wind model for simulation of thrust variations on a wind turbine, *Energy Procedia* 94 (2016) 306–318.
- [12] Caselitz, P. and Kleinkauf, W. and Krueger, T. and Petschenka, J. and Reichard, M. and Strzel, K., Reduction of fatigue loads on wind energy converters by advanced control methods, In Proceedings of European Wind Energy Conference Dublin, Ireland, 1997, pp.555–558.
- [13] L. Y. Pao, K. E. Johnson, A tutorial on the dynamics and control of wind turbines and wind farms, In Proceedings of American Control Conference St. Louis, MO, USA, July 2009.
- [14] R. J. A. M. Stevens, C. Meneveau, Temporal structure of aggregate power fluctuations in large-eddy simulations of extended wind farms, *J. Renew. Sustain. Energy* 6 (2014) 043102.
- [15] S. Frandsen, Turbulence and Turbulence-generated Structural Loading in Wind Turbine Clusters, PhD Thesis, Risø National Laboratory DTU, Roskilde, Denmark, Denmark (2007).
- [16] H. Neustadter, D. Spera, Method for evaluating wind turbine wake effects on wind farm performance, *J. Sol. Eng.* 107 (1985) 240–243.
- [17] R.J. Barthelmie and S.T. Frandsen and M.N. Nielsen and S.C. Pryor and P. Rethore and H.E. Jørgensen, Modelling and measurements of power losses and turbulence intensity in wind turbine wakes at middelgrunden offshore wind farm., *Wind Energy* 10 (6) (2007) 517–528.
- [18] F. Porté-Agel, M. Bastankhah, S. Shamsoddin, Wind-Turbine and Wind-Farm Flows: A Review, *Boundary-Layer Meteorology* 174 (2020) 1–59.

- [19] F. Porté-Agel, Y. Wu, C. Chen, A numerical study of the effects of wind direction on turbine wakes and power losses in a large wind farm, *Energies* 6 (10) (2013) 5297–5313.
- [20] K. Hansen, R. Barthelmie, L. Jensen, A. Sommer, The impact of turbulence intensity and atmospheric stability on power deficits due to wind turbine wakes at horns rev wind farm, *Wind Energy* 15 (1) (2012) 183–196.
- [21] K. B. Howard, J.S.Hu, L. P. Chamorro, M. Guala1, Characterizing the response of a wind turbine model under complex inflow conditions, *Wind Energy* 18 (2015) 729–743.
- [22] L. Chamorro, C. Hill, S. Morton, C. Ellis, R. Arndt, F. Sotiropoulos, On the interaction between a turbulent open channel flow and an axial-flow turbine, *Journal of Fluid Mechanics* 716 (2013) 658–670.
- [23] L. Chamorro, C. Hill, V. S. Morton, B. Gunawan, R. E. A. Arndt, F. Sotiropoulos, Effects of energetic coherent motions on the power and wake of an axial-flow turbine, *Physics of Fluids* 27 (2015) 055104.
- [24] G. S. Payne, T. Stallard, R. Martinez, T. Bruce, Variation of loads on a three-bladed horizontal axis tidal turbine with frequency and blade position, *Journal of Fluids and Structures* 83 (2018) 156–170.
- [25] A. Jimenez, A. Crespo, E. Migoya, J. Garcia, Advances in large eddy simulation of a wind turbine wake, *J. Phys. Conf. Ser.* 75 (1) (2007) 012041.
- [26] Z. Yang, Large eddy simulation: Past, present and the future, *Chinese Journal of Aeronautics* 28 (2015) 11–24.
- [27] M. Calaf, C. Meneveau, J. Meyers, Large eddy simulation study of fully developed wind turbine array boundary layers, *Phys. Fluids* 22 (1) (2010) 015110.
- [28] J. N. Sørensen, C. W. Kock, A model for unsteady rotor aerodynamics, *J. Wind Eng. Ind. Aerodyn* 58(3) (1995) 259–275.
- [29] C. Masson, A. Smali, C. Leclerc, Aerodynamic analysis of HAWTs operating in unsteady conditions, *Wind Energy* 4 (1) (2001) 1–22.
- [30] N. Troldborg, Actuator Line Modelling of Wind Turbine Wakes, PhD Thesis, Technical University of Denmark, Denmark (2008).
- [31] R. J. A. M. Stevens, L. A. Martínez-Tossas, C. Meneveau, Comparison of wind farm large eddy simulations using actuator disk and actuator line models with wind tunnel experiments, *Renew. Energy* 116 (2018) 470–478.
- [32] M. H. B. Ahmadi, P. Dong, Validation of the actuator line method for simulating flow through a horizontal axis tidal stream turbine by comparison with measurements, *Renew. Energy* 113 (2017) 420–427.
- [33] M. H. B. Ahmadi, P. Dong, Numerical simulations of wake characteristics of a horizontal axis tidal stream turbine using actuator line model, *Renew. Energy* 113 (2017) 669–678.
- [34] S. Menon, P. K. Yeung, W. W. Kim, Effect of Subgrid Models on the Computed Interscale Energy Transfer in Isotropic Turbulence, *Computers & Fluids* 25 (2) (1996) 165–180.
- [35] OpenFOAM, Released via the OpenFOAM Foundation, See <http://openfoam.org>.
- [36] J. N. Sørensen, W. Z. Shen, Numerical Modelling of Wind Turbine Wakes, *Journal of Fluids Engineering* 124 (2002) 393–399.
- [37] W. Z. Shen, W. J. Zhu, J. N. Sørensen, Actuator Line/Navier-Stokes Computations for The MEXICO Rotor: Comparison With Detailed Measurements, *Wind Energy* 15(5) (2012) 811–825.
- [38] J. Schepers, H. Snel, Mexico, model experiments in controlled conditions, Tech. Rep. ECNE-07-042, Energy Research Center of the Netherlands (2007).
- [39] K. Boorsma, J. G. Schepers, Description of experimental setup, MEXICO measurements, Tech. Rep. ECN-X-09-0XX, ECN (2009).
- [40] K. Nilsson, W. Z. Shen, J. N. Sørensen, S. P. Breton, S. Ivanell, Validation of the actuator line method using near wake measurements of the MEXICO rotor, *Wind Energy* 37 (3) (2015) 499–514.
- [41] A. Chaudhari, Large eddy simulation of wind flows over complex terrains for wind energy applications, Ph.D. Thesis, Lappeenranta University of Technology, Lappeenranta, Finland 2014.
- [42] M. H. B. Ahmadi, Z. Yang, The evolution of turbulence characteristics in the wake of a horizontal axis tidal stream turbine, *Renew. Energy* 151 (2020) 1008–1015.